Proceedings of the
Annual Stability Conference
Structural Stability Research Council
Atlanta, Georgia, April 21-24, 2026

Cross-sectional behavior of aluminium alloy irregular rectangular hollow section stub columns after exposure to fire

Wen Cheng[1], Kang Chen[2], Yao Sun[3]

Abstract

This study investigates the post-fire behavior and compressive strength of aluminum alloy stub columns with irregular rectangular hollow sections (IRHS), a design increasingly used in prefabricated aluminum structures such as modular housing and temporary shelters. The study examines four IRHS profiles and includes specimen heating and cooling tests, 16 post-fire material tests and 32 post-fire stub column tests. The design analysis indicates that international codes are generally accurate for post-fire design of aluminum IRHS stub columns exposed to temperatures below 200 ºC. However, they tend to be overly conservative when temperatures exceed 300 ºC, as they do not account for the significant strain-hardening of the material. Compared to international codes, the continuous strength method improves the accuracy of post-fire design for aluminum IRHS across the full temperature range, as it incorporates material hardening after fire exposure.

1. Introduction

Aluminum alloys have found wide applications in structural and bridge engineering, due to their lightweight nature, high strength-to-weight ratio, excellent corrosion resistance and ease of fabrication (Sun 2023). Moreover, aluminum is a sustainable material in construction, as structural aluminum can be recycled without degradation of physical and chemical properties (Sun 2025), promoting a circular economy and reducing environmental impact. Extensive research has been conducted on structural aluminum with a wide range of material grades and cross-sectional profiles, to investigate their structural performance at the cross-section levels. These studies aimed at assessing the structural performance of aluminum elements, evaluating the accuracy of current design specifications and proposing more appropriate design approaches. Several stub column testing programmes have been conducted on doubly symmetric sections, including circular (Feng et al. 2016), rectangular (Faella et al. 2000) and square (Feng et al. 2016, Maljaars et al. 2009, Faella et al. 2000) hollow sections (i.e. CHS, RHS and SHS) and I-section (Zhi et al. 2022, Yuan et al. 2015), to explore their local stability and cross-sectional strengths. Most tested stub columns failed due to significant local buckling, and the measured compressive strengths were used to examine EN 1999-1-1 (CEN 2013) and ADM (AA 2020). The cross-sectional response of

[1] PhD candidate, Xi'an Jiaotong-Liverpool University, Suzhou 215123, China <wencheng@liverpool.ac.uk>
[2] Assistant Professor, Xi'an Jiaotong-Liverpool University, Suzhou 215123, China <kang.chen@xjtlu.edu.cn>
[3] Full Professor, Hunan University, Changsha 410082, China <yaosun@hnu.edu.cn>

monosymmetric (e.g. Tee (Yuan and Zhang 2022), channel (Sun et al. 2023, Georgantzia et al. 2023) and equal-leg angle (Maljaars et al. 2009, Sun et al. 2024a)) and asymmetric (e.g. unequal-leg angle (Sun et al. 2024a)) sections was also experimentally investigated. Comparisons with codified provisions generally showed slightly conservative predictions and improved approaches, represented by the continuous strength method (Gardner et al. 2023), were devised to more accurately predict compressive strengths under local buckling.

The review also indicates that most previous studies focus on regular cross-sectional profiles, while limited research is available for irregular-profiled counterparts. Irregular-profiled aluminum components are increasingly adopted in practice, such as prefabricated assembled tents composed of irregular rectangular hollow section (IRHS) aluminum components (see Fig. 1), widely used for exhibitions, temporary shelters and emergency relief operations. In these applications, fire risks can be higher due to makeshift electrical setups and unpredictable environmental conditions. When exposed to fire (Liu et al. 2025), aluminum structures heat up rapidly, leading to significant degradation of mechanical properties, particularly stiffness and strength (Sun et al. 2023a, 2024c). In the post-fire scenario, several studies have been conducted on aluminum channel (Sun et al. 2023b), angle (Sun et al. 2024b, 2025a), SHS (Sun et al. 2025b, Sun and Han 2025a), SHS (Sun and Han 2025b) and CHS (Sun et al. 2025c) stub columns, highlighting conservatism in international design guidelines (CEN 2013, AA 2020). Moreover, Jiang et al. (2021) investigated the blast damage effects on the post-fire aluminum CHS components and proposed a spatial surface function to capture the corresponding response. However, the post-fire structural performance of irregular-profiled aluminum components remains unexplored.

To quantify post-fire damage in structural aluminum components with irregular profiles, a comprehensive testing project is underway at Xi'an Jiaotong-Liverpool University. This paper presents heating tests, 16 post-fire coupon tests and 32 post-fire stub column tests on grade 6061-T6 aluminum IRHS and compares the results with predictions from design codes (CEN 2013, AA 2020) and the CSM (Gardner et al. 2023).

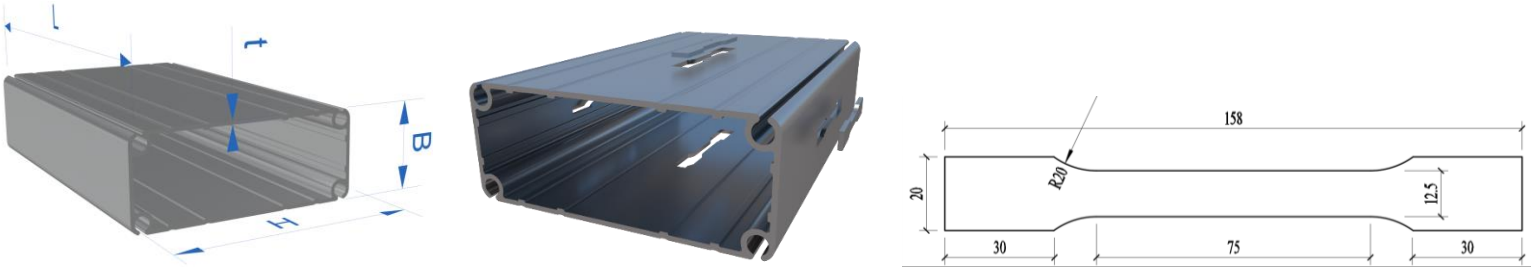

(a) Notations of IRHS. (b) Extraction of coupons. (c) Coupon size.

Figure 1: Graphical illustration of IRHS and coupon.

2. Testing Programme

A series of tests was carried out to examine the post-fire behavior and residual strength of aluminum IRHS stub columns. Four 6061-T6 sections with two wall thicknesses were used, including IRHS 350×120×5, 300×120×5, 252×112×4 and 203×112×4. The members were fabricated in accordance with EN 755-1 (CEN 2016). In total, 32 stub columns were prepared, with eight specimens for each section. To characterise the material properties, tensile coupons were also taken from the IRHS using wire electrical discharge machining. Eight coupons were extracted for each thickness (4 and 5 mm), giving 16 coupons overall. The coupon dimensions

followed EN ISO 6892-1 (CEN 2019), as shown in Fig. 1. The programme included specimen heating, post-fire coupon tests and post-fire stub-column tests.

2.1 Specimens heating

To acquire post-fire stub columns and coupons, an electric furnace was adopted to heat the prepared specimens. In the heating process, 8 different temperature levels were prespecified, including the ambient temperature of 25 ºC and 7 elevated temperatures of 100 ºC, 200 ºC, 300 ºC, 350 ºC, 400 ºC, 500 ºC and 550 ºC. Given the fact that the aluminum melting point is approximately 600 ºC to 650 ºC (Sun 2023), the highest prespecified temperature was thus limited to 550 ºC to prevent the occurrence of molten aluminum state. As displayed in Fig. 2, the electric furnace chamber contains a collection of heating elements that are distributed uniformly to ensure consistent and controlled heating throughout the furnace.

The specimens were gradually heated from ambient temperature to each prespecified temperature at a controlled heating rate of 15 °C/min (Chen and Sun 2025a). During the heating process, six thermocouples were strategically tied to specimens to provide real-time monitoring (Sun et al. 2025d) of the temperature distribution of the specimens. Once the pre-specified temperature was attained, it was maintained at a constant value for a 60-minute soaking period to ensure a stable and uniform temperature distribution throughout each specimen. The furnace was then switched off, allowing the specimens to cool naturally. Fig. 3 depicts the temperature versus time histories monitored for the prespecified temperature of 300 ºC. The figure shows that the near-coincidence of the temperature–time curves, confirming that the temperature was uniformly distributed within the furnace and across the specimens during the whole process. The maximum temperatures recorded by each thermocouple were averaged to provide an accurate representation of the temperature conditions experienced by the specimens, as denoted as "*T*" and tabulated in Table 1.

(a) Opening. (b) Closure.

Figure 2: Electric furnace.

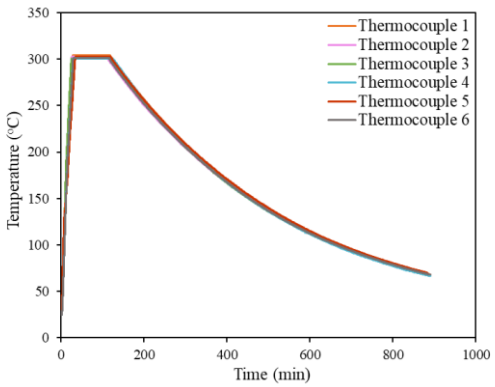

Figure 3: Measured temperature–time histories for 300 ºC.

Table 1: Measured post-fire material properties of aluminum alloy 6061-T6.

Coupon thickness	T (ºC)	E (GPa)	f_o (MPa)	f_u (MPa)	ε_f (%)	f_u/f_o
5 mm	25	71.1	241.8	287.5	10.5	1.19
	105	70.6	240.2	289.2	10.5	1.20
	203	70.5	251.3	284.1	6.8	1.13
	304	70.7	134.3	191.7	13.9	1.43
	351	70.8	98.0	162.7	13.5	1.66
	402	70.9	46.9	123.6	28.4	2.63

	501	70.8	40.7	115.8	28.6	2.85
	552	71.0	40.3	124.0	29.5	3.08
4 mm	25	70.5	240.9	276.1	6.8	1.15
	105	70.7	245.8	276.8	7.3	1.13
	203	70.6	249.7	279.8	7.2	1.12
	304	70.2	129.1	187.6	11.8	1.45
	351	70.9	86.7	155.0	13.4	1.79
	402	71.2	35.6	120.3	33.5	3.38
	501	70.8	34.5	112.3	33.6	3.26
	552	69.9	38.1	116.1	27.6	3.04

2.2 Post-fire material testing

To derive the post-fire material responses of the aluminum used, material testing was undertaken on the post-fire coupons. All the 16 post-fire coupons were tested in a 100 kN INSTRON 5982 universal machine, which applied tensile loading onto the coupons. The tensile loading was applied subject to a displacement-controlled scheme, with the loading rate initially set as 0.05 mm/min and changed to 0.80 mm/min upon attainment of 0.2% proof strength (Chen and Sun 2025b, Ran et al. 2023, 2024a). As shown in Fig. 4, tensile strains and elongations were measured using a Digital Image Correlation (DIC) system. Two high-speed cameras were placed at optimised angles and calibrated before testing to enable accurate reconstruction of surface deformation. During each coupon test, synchronised images were recorded throughout loading and processed by the DIC software to track surface displacements between consecutive frames (Chen et al. 2025, Oluwadahunsi and Sun 2026). Longitudinal tensile strains were then obtained from these displacements with sub-pixel accuracy.

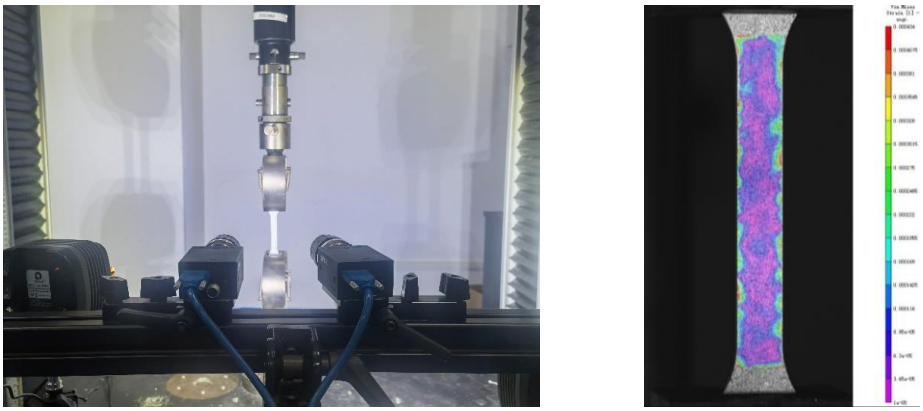

(a) Global view. (b) DIC strain field.

Figure 4: Post-fire coupon test rig.

Figs. 5(a) and 5(b) display the post-fire stress–strain histories acquired from the material testing on the 5 mm and 4 mm thick tensile coupons, respectively. The post-fire material properties, comprising the ultimate strength f_u, the 0.2% proof strength f_o, the Young's modulus E and the fracture strain ε_f, are summarised in Table 1. Both Fig. 5 and Table 1 reveal that the exposure temperatures can affect the post-fire material response significantly. Table 1 also reports the ultimate-to-yield strength ratios f_u/f_o, which are graphically plotted against the elevated temperatures in Fig. 6. It can be seen from the figure and the table that (i) when the exposure

temperatures are below 200 °C, the post-fire material coupons exhibit insignificant strain-hardening effect (i.e. the post-fire f_u/f_o ratios are quite similar to the ambient-temperature f_u/f_o ratios), (ii) but the strain-hardening effect becomes rather distinct as the exposure temperatures are above 300 °C, as the post-fire f_u/f_o ratios are greater than 1.40.

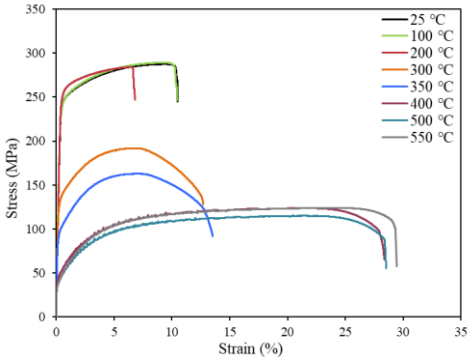

(a) 5mm-thick coupons.

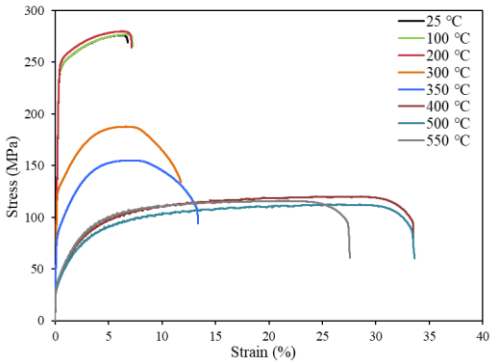

(b) 4mm-thick coupons.

Figure 5: Measured post-fire stress–strain curves.

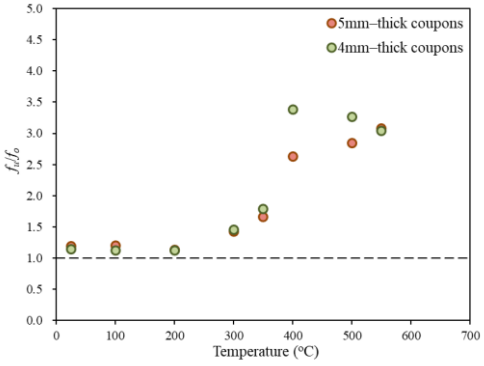

Figure 6: Effect of exposure temperature on material hardening.

2.3 Post-fire stub column tests

Concentric compression tests were performed on the 32 post-fire aluminium IRHS stub columns, to investigate their cross-sectional behaviour and residual compressive capacity after exposure to elevated temperatures. Before testing, the geometric dimensions of the stub column specimens were carefully measured, as summarised in Table 2, involving the section outer height H, the section outer width B, the plate thickness t and the member length L; these geometric notations have also been depicted in Fig. 1. It should be noted that each test specimen is labelled by its cross-sectional profile, followed by a number denoting the nominal target temperature. Each stub column test was conducted in the TYE-3000 testing machine (see Fig. 7), which applied axial compression with fixed-end conditions. A loading rate of 0.2 mm/min (Ran et al. 2024b, Sun and Chen 2025, Yang and Sun 2026) was adopted for driving the testing machine to uniformly compress the stub columns. A DIC system (see Fig. 7(a)) was employed to measure the compressive strains during testing, with a representative strain field captured by the DIC system displayed in Fig. 7(b).

Table 2: Geometries of post-fire IRHS stub columns.

Cross-section	Specimen ID	L (mm)	B (mm)	H (mm)	t (mm)
IRHS-350×120×5	IRHS-350×120×5-T25	449.8	349.85	120.23	4.99
	IRHS-350×120×5-T100	450.1	349.92	119.89	4.98
	IRHS-350×120×5-T200	449.6	350.40	119.95	4.96
	IRHS-350×120×5-T300	450.3	349.82	120.06	4.99
	IRHS-350×120×5-T350	449.9	349.64	120.09	4.89
	IRHS-350×120×5-T400	449.7	349.85	119.86	4.97
	IRHS-350×120×5-T500	450.2	350.40	120.13	4.93
	IRHS-350×120×5-T550	449.5	349.95	119.95	5.02
IRHS-300×120×5	IRHS-300×120×5-T25	399.8	300.12	119.94	4.95
	IRHS-300×120×5-T100	400.1	299.86	120.07	5.01
	IRHS-300×120×5-T200	399.6	299.93	120.11	5.07

	IRHS-300×120×5-T300	400.3	300.06	120.13	4.99
	IRHS-300×120×5-T350	399.9	299.98	119.88	4.97
	IRHS-300×120×5-T400	399.7	300.01	119.97	5.02
	IRHS-300×120×5-T500	400.2	300.13	120.06	4.98
	IRHS-300×120×5-T550	399.5	299.96	119.99	4.97
IRHS-252×112×4	IRHS-252×112×4-T25	324.8	252.18	112.11	3.91
	IRHS-252×112×4-T100	325.1	252.09	112.08	3.98
	IRHS-252×112×4-T200	324.8	252.14	112.04	3.95
	IRHS-252×112×4-T300	325.3	252.03	112.21	3.97
	IRHS-252×112×4-T350	324.9	252.07	112.09	3.94
	IRHS-252×112×4-T400	325.2	252.23	112.04	4.01
	IRHS-252×112×4-T500	325.1	251.97	111.99	4.02
	IRHS-252×112×4-T550	324.7	252.96	112.07	3.99
IRHS-203×112×4	IRHS-203×112×4-T25	300.3	203.13	112.01	3.99
	IRHS-203×112×4-T100	300.6	203.07	112.09	3.98
	IRHS-203×112×4-T200	300.0	203.05	112.14	3.96
	IRHS-203×112×4-T300	300.1	202.96	112.03	3.97
	IRHS-203×112×4-T350	299.8	202.95	112.06	4.03
	IRHS-203×112×4-T400	299.6	203.09	112.13	3.99
	IRHS-203×112×4-T500	300.5	203.12	112.08	3.92
	IRHS-203×112×4-T550	300.5	202.91	111.96	3.95

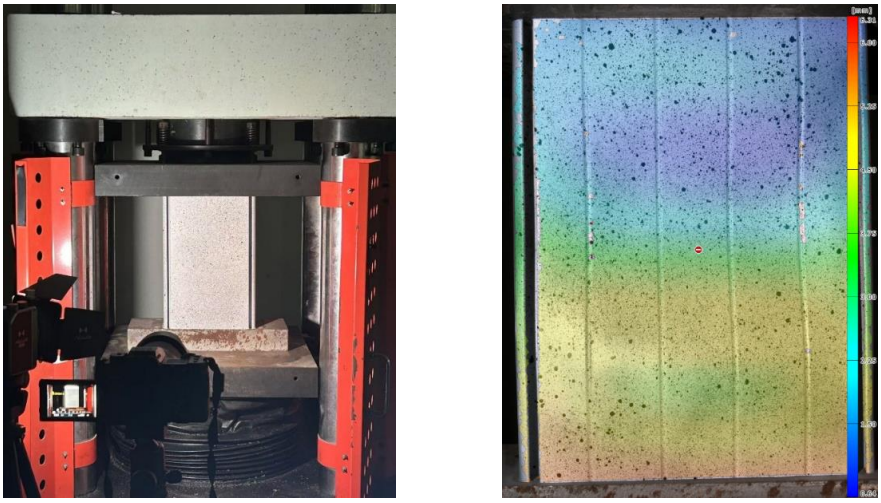

(a) Global view. (b) DIC strain field.

Figure 7: Post-fire stub column test rig.

Upon testing, all the 32 tested post-fire aluminium IRHS stub columns were observed to fail by local buckling. Figs. 8(a)–8(d) depict the full load–end-shortening histories for the four groups of IRHS stub columns, whilst Table 3 summarises the key experimental results, involving the post-fire failure loads N_u, the corresponding end-shortenings δ_u and the post-fire ultimate-to-yield load ratios $N_u/(Af_o)$. The table also reports the ratio of the post-fire ultimate load to the ambient-temperature value $N_u/N_{u,25}$. With reference to the data presented, it is evident that for the four specimen groups, the load capacities were relatively unaffected following exposure to temperatures of 200 °C, then reduced significantly after heating to 300 °C and reduced

significantly again following exposure to 400 ºC. Thereafter, the reductions in load capacity were relatively constant. Fig. 9 plots ultimate-to-yield load ratios $N_u/(Af_o)$ versus exposure temperature, showing that the ratio generally increases with temperature. The trend pattern of $N_u/(Af_o)$ shown in Fig. 9 is consistent with the f_u/f_o trend shown in Fig. 6, indicating that the variation in load ratios is mainly due to strain hardening.

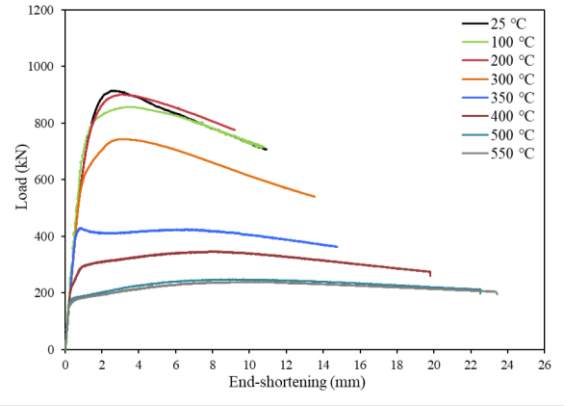

(a) IRHS-350×120×5 specimens.

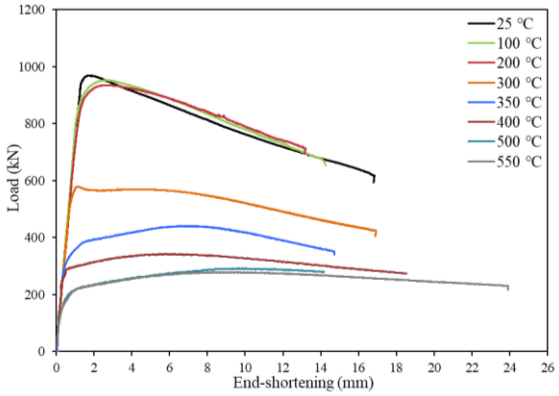

(b) IRHS-300×120×5 specimens.

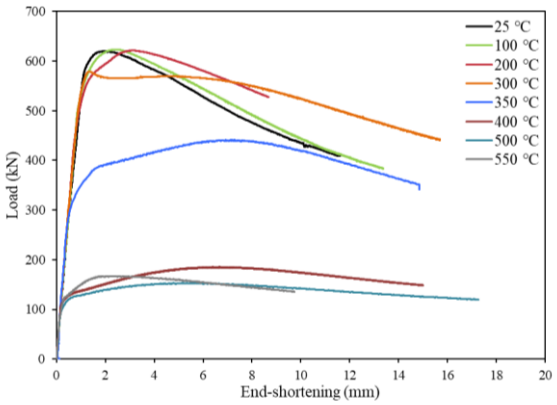

(c) IRHS-252×112×4 specimens.

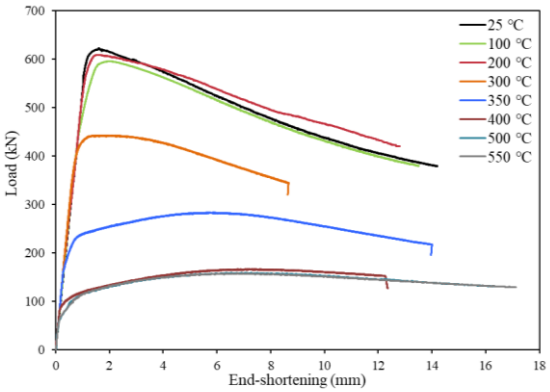

(b) IRHS-203×112×4 specimens.

Figure 8: Test load–end-shortening curves of post-fire IRHS stub columns.

Table 3: Key test results for post-fire IRHS stub columns.

Cross-section	Specimen ID	N_u (kN)	δ_u (mm)	$N_u/(Af_o)$	$N_u/N_{u,25}$
IRHS-350×120×5	IRHS-350×120×5-T25	914.26	2.68	0.708	1
	IRHS-350×120×5-T100	856.89	3.55	0.668	0.937
	IRHS-350×120×5-T200	900.84	3.07	0.671	0.985
	IRHS-350×120×5-T300	743.62	3.16	1.037	0.813
	IRHS-350×120×5-T350	429.52	0.84	0.821	0.470
	IRHS-350×120×5-T400	346.55	7.92	1.383	0.379
	IRHS-350×120×5-T500	247.72	8.88	1.140	0.271
	IRHS-350×120×5-T550	239.25	10.59	1.111	0.262
IRHS-300×120×5	IRHS-300×120×5-T25	968.63	1.73	0.827	1
	IRHS-300×120×5-T100	952.45	2.58	0.819	0.983
	IRHS-300×120×5-T200	935.00	2.83	0.769	0.965

	IRHS-300×120×5-T300	579.20	1.14	0.891	0.598
	IRHS-300×120×5-T350	441.16	7.04	0.930	0.455
	IRHS-300×120×5-T400	342.46	5.54	1.508	0.354
	IRHS-300×120×5-T500	291.78	9.68	1.481	0.301
	IRHS-300×120×5-T550	278.70	8.96	1.428	0.288
IRHS-252×112×4	IRHS-252×112×4-T25	620.81	2.09	0.789	1
	IRHS-252×112×4-T100	623.41	2.38	0.776	1.004
	IRHS-252×112×4-T200	621.51	3.12	0.762	1.001
	IRHS-252×112×4-T300	579.20	1.35	1.373	0.933
	IRHS-252×112×4-T350	441.16	7.18	1.557	0.711
	IRHS-252×112×4-T400	185.71	6.69	1.596	0.299
	IRHS-252×112×4-T500	153.07	5.33	1.358	0.247
	IRHS-252×112×4-T550	167.16	2.40	1.342	0.269
IRHS-203×112×4	IRHS-203×112×4-T25	622.44	1.60	0.904	1
	IRHS-203×112×4-T100	595.64	1.96	0.848	0.957
	IRHS-203×112×4-T200	609.17	1.61	0.854	0.979
	IRHS-203×112×4-T300	442.63	1.78	1.200	0.711
	IRHS-203×112×4-T350	283.55	5.68	1.145	0.456
	IRHS-203×112×4-T400	166.77	7.21	1.639	0.268
	IRHS-203×112×4-T500	159.15	7.08	1.614	0.256
	IRHS-203×112×4-T550	157.67	6.98	1.448	0.253

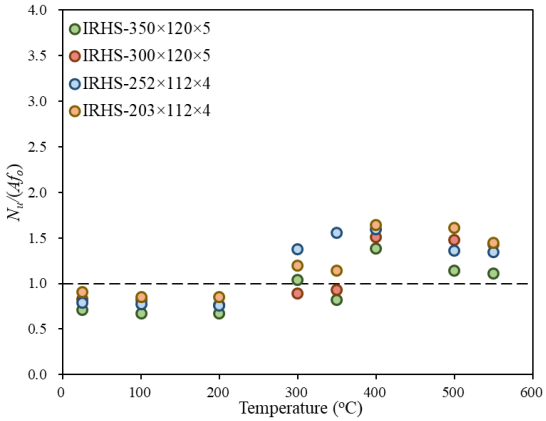

Figure 9: Effect of exposure temperatures on $N_u/(Af_o)$ load ratios of post-fire IRHS stub columns.

3. Design Analysis

Upon completion of the laboratory testing, a systematic design analysis is conducted in this section. The ambient-temperature design provisions for aluminum IRHS in compression, as prescribed in EN 1999-1-1 (CEN 2013), ADM (AA 2020) and the CSM (Gardner et al. 2023), were firstly described and discussed. The applicability of each ambient-temperature design approach to post-fire conditions was examined by comparing the measured post-fire failure loads N_u, with the corresponding unfactored post-fire capacity predictions $N_{u,pred}$. Table 4 reports the mean test-to-predicted capacity ratio for each approach, whilst Figs. 10–13 display the graphical assessments, in which the capacity ratios are plotted against the exposure temperatures.

Table 4: Mean test-to-predicted ratios for examined design approaches.

Temperature	$N_u/N_{u,EC9}$	$N_u/N_{u,ADM}$	$N_u/N_{u,CSM}$
25 ºC	1.092	1.079	1.217
100 ºC	1.054	1.042	1.176
200 ºC	1.040	1.029	1.171
300 ºC	1.380	1.354	1.216
400 ºC	1.281	1.269	1.067
450 ºC	1.605	1.673	1.220
500 ºC	1.467	1.504	1.141
550 ºC	1.399	1.435	1.122
Overall	1.290	1.298	1.166

3.1 EN 1999-1-1 (EC9)

The Eurocode EN 1999-1-1 (CEN 2013) is established specifically for the design of structural aluminum components at ambient temperature. To use EN 1999-1-1 (CEN 2013) to calculate the design capacity of an aluminum stub column, the first step lies in the classification of the cross-section. For cross-sections in compression, EN 1999-1-1 (CEN 2013) categorises them into non-slender (Class 1–3) and slender (Class 4) sections (Yang et al. 2025); its class is dependent on the width-to-thickness ratio of each flat plate element. Regarding IRHS used in this study, a series of longitudinal ribs can be seen. These ribs might not be considered as stiffeners that can enhance the cross-sectional capacity, since the depth of the rib is less than the rib thickness but EN 1999-1-1 (CEN 2013) only considers the ribs with the depth-to-thickness ratio greater than unity as effective. Therefore, the class of IRHS was determined based on the width-to-thickness ratios ($\beta = (H–2t)/t$ or $\beta = (B–2t)/t$) of the four faces. Upon completion of the cross-section classification, EN 1999-1-1 (CEN 2013) prescribes the cross-sectional yield load Af_o and effective load $A_{eff}f_o$ as the design compressive capacities $N_{u,EC9}$ for non-slender IRHS and slender IRHS, respectively. A and A_{eff} represent the gross and effective sectional areas, respectively, with the latter derived from the effective thickness concept accounting for local buckling effect. Specifically, the effective plate thickness t_{eff} is calculated as the original thickness t multiplied by a reduction factor ρ_c – see Eq. (1), where ρ_c is determined from Eq. (2). Upon determination of the effective thicknesses, the effective area A_{eff} is taken as the sum of the areas of the four plates with effective thicknesses.

$$t_{eff} = \rho_c t \tag{1}$$

$$\rho_c = \frac{32}{\beta/\sqrt{250/f_o}} - \frac{220}{\left(\beta/\sqrt{250/f_o}\right)^2} \tag{2}$$

Based on the obtained test data, the suitability of the EC9 room-temperature design provisions (CEN 2013) for post-fire aluminum IRHS stub columns is assessed. A quantitative assessment is performed firstly, with the results, comprising the mean test-to-predicted capacity ratio $N_u/N_{u,EC9}$, reported in Table 4. As given in Table 4, the mean $N_u/N_{u,EC9}$ post-fire capacity ratios are 1.092, 1.054 and 1.040 for the exposure temperatures of 25 ºC, 100 ºC and 200 ºC, revealing a high level of design accuracy for this temperature range. However, excessive under-estimations of the post-fire capacities are observed for the exposure temperatures ranging from 300 ºC to 550 ºC, as reflected by the mean $N_u/N_{u,EC9}$ capacity ratios of 1.380–1.605. The $N_u/N_{u,EC9}$ capacity ratios are plotted against the exposure temperatures in Fig. 10. It indicates that EN 1999-1-1 (CEN 2013) generally yields safe post-fire compressive capacity predictions for aluminum IRHS, with a high level of post-fire design accuracy for members following exposure to relatively low levels of

elevated temperature. However, for exposure temperatures above 300 °C, the predicted post-fire capacities of the IRHS stub columns become overly conservative. This is primarily attributable to the omission of the pronounced strain-hardening response.

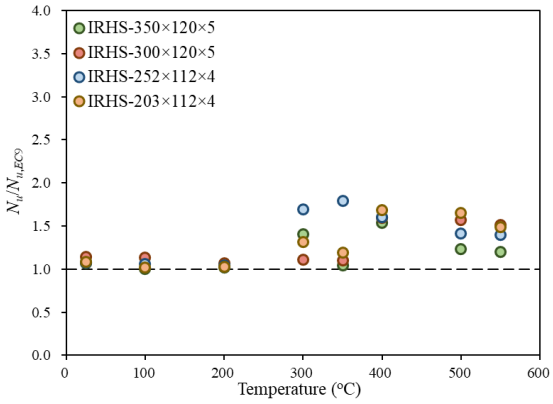

Figure 10: Comparisons of test and EN 1999-1-1 failure loads.

3.2 ADM 2020

ADM 2020 (AA 2020) is an aluminum design manual used in the United States. For IRHS in compression, ADM 2020 (AA 2020) uses the weighted average approach to predict the compressive capacity $N_{u,ADM}$, as expressed by Eq. (3), in which A_i is the area of the i^{th} constituent plate, $f_{c,i}$ denotes the corresponding buckling stress, as calculated from Eq. (4), where B_p and D_p are the buckling constants, as derived from Eqs (5) and (6), respectively.

$$N_{u,ADM} = \sum_{i=1}^{4} f_{c,i} A_i + f_o \left(A - \sum_{i=1}^{4} A_i \right) \tag{3}$$

$$f_c = \begin{cases} f_o & \text{for } \beta \le \dfrac{B_p - f_o}{1.6 D_p} \\ B_p - 1.6 D_p \beta & \text{for } \dfrac{B_p - f_o}{1.6 D_p} < \beta < \dfrac{0.35 B_p}{1.6 D_p} \\ \dfrac{2.27\sqrt{B_p E}}{1.6\beta} & \text{for } \beta \ge \dfrac{0.35 B_p}{1.6 D_p} \end{cases} \tag{4}$$

$$B_p = f_o \left[1 + \left(\frac{f_o}{10343} \right)^{\frac{1}{3}} \right] \tag{5}$$

$$D_p = \frac{B_p}{10} \cdot \sqrt{\left(\frac{B_p}{E} \right)} \tag{6}$$

The test post-fire capacities are compared to the values predicted by ADM 2020 (AA 2020) to assess their applicability for aluminum IRHS stub columns after exposure to fire. The results are graphically presented in Fig. 11, where the test post-fire capacities N_u are normalised by the corresponding $N_{u,ADM}$ and plotted against the exposure temperatures. It is observed that the design provisions offer reasonable accuracy for predicting the capacities of aluminum IRHS after elevated

temperature exposures between 25 ºC and 200 ºC. However, following exposure to higher levels of temperature between 300 ºC and 550 ºC, the design codes tend to underestimate the post-fire capacity quite considerably. Table 4 also includes the mean $N_u/N_{u,ADM}$ load ratios for the exposure temperatures and the results indicate a similar level of post-fire design accuracy to that of EN 1999-1-1 (CEN 2013).

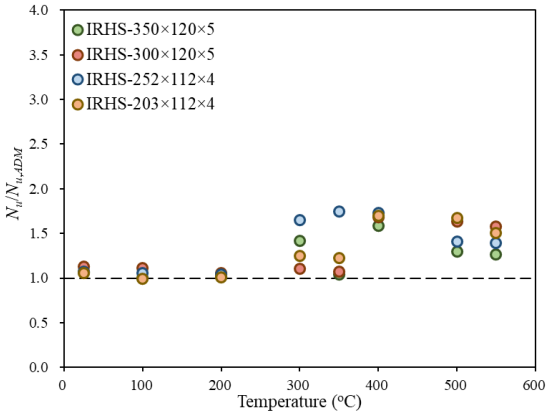

Figure 11: Comparisons of test and ADM 2020 failure loads.

3.3 CSM

The results presented in previous sections show that the existing international codes (CEN 2013, AA 2020) offer conservative capacity predictions for post-fire aluminum IRHS stub columns when the exposure temperatures are above 300 ºC. To overcome the design conservatism, the CSM (Gardner et al. 2023) that properly accounts for strain-hardening is considered herein. To calculate the CSM cross-sectional capacity, the first step is the determination of the CSM strain limit ε_{csm} that measures the cross-sectional deformation capacity. This can be completed by utilising the "base curve", given in Eq. (7), in which $\varepsilon_y = f_o/E$ is the yield strain, $\lambda_{p,cs}=(f_o/f_{cr,cs})^{0.5}$ denotes the cross-sectional slenderness, in which $f_{cr,cs}$ is the elastic local buckling stress of IRHS, as derived using the finite-strip programme CUFSM (Schafer and Adany 2006). Upon quantifying the CSM strain limit ε_{csm}, the CSM compressive capacity $N_{u,CSM}$ is calculated from Eq. (8), in which E_{sh} is the strain-hardening modulus, expressed in Eq. (9), where $\varepsilon_{u,csm} = 0.13(1–f_o/f_u)+0.06$ denotes the CSM ultimate strain.

$$\frac{\varepsilon_{csm}}{\varepsilon_y} = \begin{cases} \dfrac{0.25}{\lambda_{p,cs}^{3.6}} \le \min\left(15, \dfrac{0.5\varepsilon_u}{\varepsilon_y}\right) & \text{for } \lambda_{p,cs} \le 0.68 \\ \left(1-\dfrac{0.222}{\lambda_{p,cs}^{1.05}}\right)\dfrac{1}{\lambda_{p,cs}^{1.05}} & \text{for } \lambda_{p,cs} > 0.68 \end{cases} \tag{7}$$

$$N_{u,CSM} = \begin{cases} Af_o \dfrac{\varepsilon_{csm}}{\varepsilon_y} & \text{for } \dfrac{\varepsilon_{csm}}{\varepsilon_y} \le 1.0 \\ Af_o + AE_{sh}\varepsilon_y\left(\dfrac{\varepsilon_{csm}}{\varepsilon_y}-1\right) & \text{for } \dfrac{\varepsilon_{csm}}{\varepsilon_y} > 1.0 \end{cases} \tag{8}$$

$$E_{sh} = \frac{f_u - f_o}{0.5\varepsilon_{u,csm} - \varepsilon_y} \tag{9}$$

The experimental ultimate loads N_u, normalised by the corresponding $N_{u,CSM}$, are plotted against exposure temperatures in Fig. 12, where the CSM (Gardner et al. 2023) is found to well predict the experimental post-fire ultimate loads. The qualitative assessment is followed by its quantitative counterpart, with the results summarised in Table 4, in which the mean $N_u/N_{u,csm}$ ratios range from 1.067 to 1.220 for the eight exposure temperatures. The assessments demonstrate that the CSM (Gardner et al. 2023) leads to greatly improved design accuracy over codes (CEN 2013, AA 2020) for aluminum IRHS stub columns for the full-range of exposure temperatures, mainly due to the rational consideration of post-fire strain-hardening.

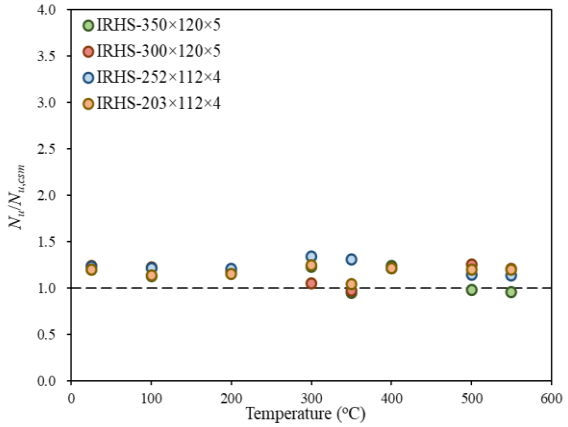

Figure 12: Comparisons of test and CSM failure loads.

4. Conclusions

The post-fire behavior and residual compressive resistance of aluminum IRHS stub columns were investigated through a systematic laboratory programme comprising specimen heating, post-fire material testing and 32 post-fire stub column tests. Following the experimental study, a design assessment was undertaken in which the compressive strength predictions from EN 1999-1-1 (CEN 2013) and ADM 2020 (AA 2020) were evaluated against the measured residual strengths, together with the Continuous Strength Method (CSM) (Gardner et al. 2023). The results show that the codified provisions generally provide satisfactory predictions for exposure temperatures between 25 ºC and 200 ºC, where post-fire strain hardening is limited, whereas they become unduly conservative at exposure temperatures above 300 ºC due to the omission of the pronounced strain-hardening effect. By contrast, because the CSM explicitly accounts for strain hardening, it was found to deliver closer agreement with the test results over the full range of exposure temperatures.

Acknowledgments

The XJTLU Research Development Funding (No.: RDF-22-02-093), the grant from the Natural Science Foundation of Hunan Province of China (No.: 2025JJ60293) and the XJTLU Postgraduate Research Scholarship (No.: PGRS2306015) are acknowledged for financial support.

References

AA (The Aluminum Association). (2020). *Aluminum Design Manual. Specification for Aluminum Structures.* Virginia, United States.

CEN (European Committee for Standardization). (2016). *Aluminium and aluminium alloys—Extruded rod/bar, tube and profiles—Part 1: Technical conditions for inspection and delivery*. EN 755-1:2016. Brussels, Belgium: CEN.

CEN (European Committee for Standardization). (2019). EN ISO 6892-1. *Metallic Matetials: Tensile Testing - Part 1: Method of Test at Room Temperature*, Brussels.

CEN (European Committee for Standardization). (2013). EN 1999-1-1-2007+A2-2013. *Eurocode 9: Design of aluminium structures – Part 1–1: General structural rules*. Brussels, Belgium.

Chen X. & Sun Y. (2025a) In-fire behavior of wire-laser additively manufactured austenitic stainless steel. *Construction and Building Materials*, 493, 143304.

Chen X. & Sun Y. (2025b) Experimental investigation of mechanical properties of 3D-printed normal-strength and high-strength steels. *Journal of Constructional Steel Research*, 234, 109773.

Chen X., Zhao O. Xu F., Zhi J. & Sun Y. (2025) Cross-sectional capacity of wire-arc additively manufactured stainless steel channel section stub columns. *Journal of Structural Engineering (ASCE)*, 151(6), 04025057.

Feng, P., Hu, L., Qian, P., & Ye, L. (2016). Compressive bearing capacity of CFRP–aluminum alloy hybrid tubes. *Composite Structures*, 140, 749-757.

Faella, C., Mazzolani, F. M., Piluso, V., & Rizzano, G. (2000). Local buckling of aluminum members: testing and classification. *Journal of Structural Engineering*, 126(3), 353-360.

Gardner, L., Yun, X., & Walport, F. (2023). The continuous strength method–Review and outlook. *Engineering Structures*, 275, 114924.

Jiang, T., Ji, C., Wang, X., Liu, Y., Gao, F., Sun, Y., Zhang, K., & Meng, L. (2021). Experimental investigation on the damage effect of 6063-T5 aluminum alloy circular tubes subjected to blast after exposure to fire. *Thin-Walled Structures*, 159, 107290.

Liu, Z., Xu, Y., Li, Z., Zhai, M., Yang, W., Lin, J. & Sun Y. (2025). Towards evidence-based fire prevention policy: Uncovering drivers of urban residential fire spread via explainable machine learning. *Developments in the Built Environment*, 100761.

Maljaars, J., Soetens, F., & Snijder, H. H. (2009). Local buckling of aluminium structures exposed to fire. Part 1: Tests. *Thin-Walled Structures*, 47(11), 1404-1417.

Oluwadahunsi S.E. & Sun Y. (2026). Testing and design of stainless-steel channel stub columns 3D-printed by wire-laser additive manufacturing (WLAM). Journal of Structural Engineering (ASCE), 152(2), 04025268.

Ran H., Shi J., Chen Z., Ma Y. OBrien E. & Sun Y. (2023) Experimental and numerical study of laser-welded stainless steel slender I-section beam-columns. *Engineering Structures*, 286, 116128.

Ran H., Wang Y., Chen Z., Chen X. & Sun Y. (2024a) Testing, modelling and design of laser-welded stainless steel slender I-section beam-column members under combined compression and major-axis bending. *Thin-Walled Structures*, 203, 112238.

Ran H., Ma J., Chen X., Sun Y., Gkantou M. & McCrum D. (2024b) Local stability of laser-welded stainless-steel T-section stub columns. *Journal of Structural Engineering (ASCE)*, 150(7), 04024062.

Schafer BW, & Ádány S (2006). Buckling analysis of cold-formed steel members using CUFSM: conventional and constrained finite strip method. *18th Internatioan Specialty Conference on Cold-Formed Steel Structures*, 39-54.

Sun, Y. (2023). The use of aluminum alloys in structures: Review and outlook. *Structures*, 57, 105290.

Sun Y. (2025). In-fire material properties of wire-arc additively manufactured 3D-printed structural aluminum alloys. *Construction and Building Materials*, 474, 140946.

Sun Y., Zhang K. & Gong G. (2023a) Material properties of structural aluminium alloys after exposure to fire. *Structures*, 55, 2105-2011.

Sun, Y., Fu, Z., Song, Y., & Xia, J. (2023b). Cross-sectional behavior of aluminum alloy channel section stub columns after exposure to fire. *Journal of Structural Engineering*, 149(7), 04023085.

Sun Y., Wang Z., Xia J. Sarquis F.R. & de Lima L.R.O. (2024a) Experimental and numerical study of aluminium alloy angle-section stub columns. *Thin-Walled Structures*, 205, 112361.

Sun, Y., Wang, Z., Xia, J., & Chen, X. (2024b). Tests, simulations and design of aluminium alloy equal-leg angle section stub columns after exposure to fire. *Engineering Structures*, 314, 118405.

Sun Y., Cheng W. & Chen K. (2024c) In-fire and post-fire material response of high-strength aluminium alloys. *Journal of Building Engineering*, 91, 109581.

Sun Y. & Chen X. (2025) Testing and design of wire-laser additively manufactured (WLAM) stainless steel angle section stub columns. *Thin-Walled Structures*, 214, 113351.

Sun Y. & Han G. (2025a) Post-fire capacity of aluminium alloy rectangular hollow sections under compression. *Engineering Structures*, 327, 119602.
Sun Y. & Han G. (2025b) Compressive capacity of post-fire 7075-T6 high-strength aluminum alloy tubes: Testing, modeling and design. *Thin-Walled Structures*, 113592.
Sun Y., Shao M. & Cashell K. (2025a) Post-fire residual capacities of aluminum alloy unequal-leg angle sections. *Journal of Structural Engineering (ASCE)*, 151(3), 04024224.
Sun Y., Li M., Chen X. & Raffoul S. (2025b) Material response and local behaviour of post-fire aluminium alloy square hollow sections. *Journal of Constructional Steel Research*, 227, 109392.
Sun Y., Cheng W., Chen K. & Di Sarno L. (2025c) Experimental and numerical study of high-strength aluminum alloy circular hollow sections after exposure to fire. *Journal of Building Engineering*, 113185
Sun Y., Zhang Q. & Raffoul S. (2025d) Physics-informed neural network for predicting hot-rolled steel temperatures during heating process. *Journal of Engineering Research*, 13, 1496-1504.
Yang P., Chen C. & Sun Y. (2025) Machine learning-based design for high-strength steel tubular section columns. *Structures*, 80, 109872.
Yang P. & Sun Y. (2026). Cross-sectional capacity of wire-laser additively manufactured (WLAM) high-strength steel angle stub columns. *Engineering Structures*, 348, 121748.
Yuan, H. X., Wang, Y. Q., Chang, T., Du, X. X., Bu, Y. D., & Shi, Y. J. (2015). Local buckling and postbuckling strength of extruded aluminium alloy stub columns with slender I-sections. *Thin-Walled Structures*, 90, 140-149.
Yuan, L., & Zhang, Q. (2022). Buckling behavior and design of concentrically loaded T-section aluminum alloy columns. *Engineering Structures*, 260, 114221.
Zhi, X., Wang, Y., Zhang, Y., Li, B., & Ouyang, Y. (2022). Study of local buckling performance of 7075-T6 high-strength aluminium alloy H-section stub columns. *Thin-Walled Structures*, 180, 109925.